BARC
NEWSLETTER

SEM micrograph of Ti₂CrV hydride

CONTENTS

This page is intentionally left blank

Evaluation of Ti$_2$CrV Alloy for Solid State Hydrogen Storage Applications

Seemita Banerjee*, Priyanka Ruz, Asheesh Kumar
Chemistry Division
Rupsha Bhattacharyya
Heavy Water Division

Abstract

Chemistry Division, BARC, has been involved in the successful development of a large variety of solid state hydrogen storage materials including metals and alloys, porous carbons, metal organic framework (MOF), chemical hydride, etc. Among the developed materials, Ti$_2$CrV alloy shows hydrogen storage capacity up to 4 wt %, under sub-atmospheric pressure and the peak temperature of desorption is 180 ^{o}C. The material has high stability and is not based on rare earth metals and hence will not face any raw material constraints for bulk production and use. Heavy Water Division, BARC, has developed hydrogen generator based on alkaline water electrolysis, capable of producing commercial grade hydrogen up to 10 Nm^3/hr under ambient conditions. In the present work a logical step has been attempted to combine these hydrogen generation and storage technologies since both have important roles to play in hydrogen energy systems and the proposed hydrogen economy. Hydrogen generators with capacities 4 NLPH and 18 NLPH, developed by HWD, were considered for this exercise. The material was tested successfully for storing hydrogen corresponding to 1 hour production by each generator.

Keywords: Solid state hydrogen storage materials, Metal Organic Framework (MOF), Alloys, Representative Alloys, Ti$_2$CrV alloy, Ti$_2$CrV hydride, Hydrogen Generators, Ti$_2$CrV - H$_2$/D$_2$ systems, MSLD.

Introduction

Use of hydrogen as an important energy carrier for the future energy systems has been widely proposed [1,2]. It is a viable alternative to currently used fossil fuel based primary energy sources. Hydrogen based energy system has become a necessity due to depleting fossil fuel reserves and increasing concerns about environmental pollution brought about by green house gases which are generated from burning fossil fuels. Apart from its direct use as an energy carrier, hydrogen has widespread applications as a raw material in the chemical, petroleum and nuclear industries and most of the demands are currently met by production of hydrogen from hydrocarbon resources.

For widespread use of hydrogen in place of more traditional fossil fuels, it is imperative to have very efficient storage and transportation systems for it. Compact, reliable, safe and cost effective storage of hydrogen is a key challenge to the extensive commercialization of fuel cell electric vehicles and other hydrogen fuel cell applications. Additionally hydrogen storage is important from the stationary energy storage point of view, particularly when considering the power to gas energy conversion systems and storing intermittently available renewable energy for use during phases of peak demand. Involvement of hydrogen in the development of fusion energy systems, where hydrogen isotopes are the potential fuels, in house utilization of hydrogen for cooling power reactor turbine generator, nuclear fuel fabrication etc., are some of the other applications which require hydrogen storage technologies.

In this context there is a growing interest to develop appropriate hydrogen storage technologies in Department of Atomic Energy.

Available technologies for hydrogen storage

The major hydrogen storage technologies that have been widely studied and are commercially available at global level are the following:

- Hydrogen storage as compressed gas in metal or fiber reinforced plastic cylinders at pressures of 150 to 700 bar
- Liquefied hydrogen storage in cryo-insulated vessels at 20-30 K
- Solid state storage based on physisorption on porous materials such as activated carbon, metal organic frameworks, zeolites, carbon nanotubes etc., at high pressure and low temperature
- Solid state storage based on chemisorption in the form of metal or alloy hydrides (Pd, U, Ti, Mg, rare earth alloys, transition metal alloys) at ambient or above ambient pressures and temperatures

The storage technologies based on last 2 classes of materials have garnered widespread attention from the scientific community in BARC.

The United States Department of Energy has put forward certain techno-commercial targets for hydrogen storage systems, particularly for vehicular applications (e.g. system should have 6.5 wt % hydrogen storage capacity, filling time of 5 minutes, etc.), which act as a generic guideline for development and comparison of different storage technologies or materials.

The selection of an appropriate storage technology for hydrogen is decided on the basis of the following criteria:

- Quantity of hydrogen to be stored.
- Intended end use- mobile/stationary & hydrogen/isotope.
- Storage time and feed hydrogen pressure.
- Absorption and desorption temperature requirement.
- Number of storing and retrieval cycles expected.

The final selection is based on thorough evaluation of all relevant techno-commercial factors, relevant to the intended purpose of hydrogen storage.

Hydrogen storage technology development at BARC: General overview

BARC, Mumbai has been engaged in the development of materials, components and systems relevant to hydrogen and hydrogen isotope storage and is briefly described below

i) Development of a wide variety of Zr, Ti, Mg based binary, ternary and quaternary alloys and composites for hydrogen storage; evaluation of thermodynamic and kinetic properties relevant to hydrogen storage; fine tuning of the properties of storage materials as per user requirement (e.g. improvement in the thermodynamics and kinetics of hydrogen storage and release, enhancement of cyclic stability of hydrogen storage materials) [3-7].

ii) Development and fundamental study on physisorption based hydrogen storage materials. These materials typically show high absorption rate, high cyclic

stability but exhibit about 2-3 wt. % hydrogen uptake capacity at 123 K [8-11].

iii) Evaluation of shelf life or long term stability of hydrogen storage materials.

iv) Computational design of novel materials for hydrogen storage [12-14].

v) Development of technologies based on solid state hydrogen storage materials (e.g. separation and purification of hydrogen from inert gas mixtures using hydrogen selective alloys and alloy based membranes, development of chromatographic columns for hydrogen isotope separation, etc.) [15, 16].

vi) Mathematical model development and simulation studies of hydrogen storage vessel performance to estimate hydriding and dehydriding times along with heating and cooling requirements for the vessel (with given dimensions) filled with a known hydride forming material [17, 18].

Subsequent sections in this report describe the joint activities carried out in the area of solid state hydrogen storage using a novel Ti based alloy by a team comprising of members from Chemistry Division and Heavy Water Division, BARC.

Joint studies by ChD and HWD: Development, characterization and testing of Ti$_2$CrV

1) Motivation

Chemistry Division, BARC has been involved in the successful development of a large variety of novel solid materials (including metals and alloys, porous carbons,

Table-1. Hydrogen storage properties of representative alloys developed in Chemistry Division

Sl. No.	Alloy	Capacity (wt%)	Condition	H$_2$ Desorption Temperature (K)	Kinetics
1	Ti$_{1-x}$VFe$_x$ (x=0, 0.1, 0.15, 0.2, 0.4)	3.7	20 bar and RT	724	200sec
2	Zr Substituted Ti$_{0.85}$VFe$_{0.15}$	3.5	25 bar and RT	723	200sec
3	Cr Substituted Ti$_{0.85}$VFe$_{0.15}$	1.51	5 bar and RT	681	-
4	Ce Substituted Ti$_{0.85}$VFe$_{0.15}$	4.02	20 bar and RT	-	120 sec
5	Zr substituted Ti-Cr-V system	3.53	25 bar and RT	700	200sec
6	V Doped ZrFe$_2$	1.85	25 bar and RT	635	-
7	**Ti$_2$CrV Alloy**	4.37	25 bar and RT	695 (456K in situ)	300 sec
8	Ti$_{2-x}$CrVM$_x$(M=Fe, Co, Ni)	3.67	20 bar and RT	620	200sec
9	Ti$_2$CrV + xZrFe$_{1.8}$V$_{0.2}$ (x=5,10, 20 at%)	3.7	5 bar and RT	434 (in situ)	>300sec
10	Ti0.32Cr0.43V0.25+xTiMn2(x= 5,10at%)	2.9	20 bar and RT	625 and 780	>300sec
11	Ti0.67Nb0.33-xFex(x=0, .13, .2)	2.62	25 bar and RT	-	>250sec
12	Mg nanoparticles/alloys	>6 wt %	20 bar and 250°C	350°C	>250sec
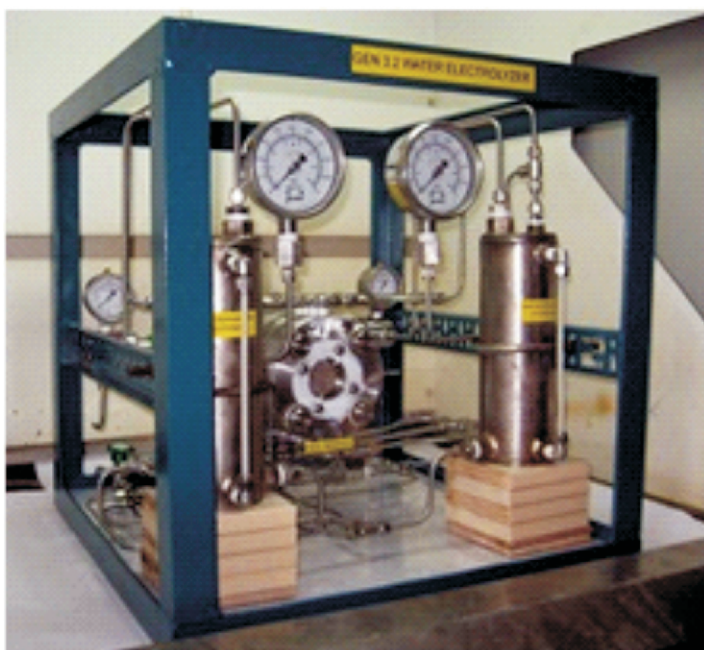
Fig.1: Table top hydrogen generator based on alkaline water electrolysis developed in Heavy Water Division, BARC

MOF, chemical hydride) for storage of hydrogen gas. Among the developed materials, one of the most promising non-rare earth metal based alloys is Ti$_2$CrV, which shows hydrogen storage capacity up to 4 wt %. under sub-atmospheric pressure and desorbs hydrogen at a temperature between 180 and 200°C. The material has high stability and is not based on rare earth metals and hence will not face any raw material constraints for bulk production and use. Hydrogen storage properties of this alloy along with other alloys developed in Chemistry Division are listed in Table -1. Heavy Water Division has developed a table top hydrogen generator based on alkaline water electrolysis (shown in Fig. 1). The generator is capable of producing commercial grade hydrogen up to 10 Nm^3/hr under ambient conditions.

Table 2: Details of joint activities carried out by ChD and HWD

Phase	Activities Performed	Remarks
1	Development and characterization of Ti$_2$CrV alloy for hydrogen storage	Alloy production process has been established. Micro-structural characteristics, elemental composition hydrogen storage and release characteristics etc. were evaluated using small quantities of sample.
2	Development and testing of vessel containing 10 gm alloy for storing 4 NL H$_2$ (commensurate with 4 NLPH H$_2$ generator)	Hydrogen storage vessel was designed, fabricated and leak testing was performed. About 10 gm of the alloy was synthesized and tested for total hydrogen storage capacity and kinetics at 4 NLPH.
3	Testing of 45 gm alloy for storing up to 18 NL hydrogen gas (commensurate with 18 NLPH H$_2$ generator)	Around 45 gm alloy was prepared in 5 batches and characterized to ensure uniformity of composition and structure across all the batches. Hydriding characteristics were evaluated under both pulsed and flow modes (at flow rates of 4 to 34 NLPH).
4	Evaluation of isotope effects in the alloy using H$_2$ and D$_2$ gases; study of long term stability of the alloy	The alloy was subjected to both hydrogen and deuterium absorption to understand the isotope effect in hydrogen storage properties. A sample of alloy, maintained under hydrogen environment for one year, was tested for its storage capacity.

It was therefore a logical step to combine these hydrogen generation and storage technologies since both have important roles to play in hydrogen energy systems and the proposed hydrogen economy. Hydrogen generators with capacities 4 NLPH and 18 NLPH, developed by HWD, were considered for this exercise. Initially the material was tested for storing hydrogen corresponding to 1 hour production by each generator. This fixed the quantity of alloy necessary for filling in to the vessel.

A phase wise plan of action was proposed as described in the next sub-section and these activities have been carried out under XII Plan sub project entitled "Laboratory Scale Studies for Hydrogen Production and Storage (88.06)" and ongoing vision project.

2) Phase wise activities

The activities carried out under this joint effort have been described in Table 2.

3) Detailed activity description

Phase 1: The alloy was synthesized in a vacuum arc melting furnace with a water cooled copper hearth under inert atmosphere of high pure Argon. A representative photo graph of the arc meting facility used for alloy preparation is shown in Fig 2. Stoichiometric amounts of the constituent elements were weighed as per the desired composition and the same was melted together to form a button. To ensure homogeneity and uniformity of composition, the alloy button was re-melted 4 times. Several characterization tests were then performed to obtain details about its structure, thermo-physical properties and hydrogen uptake and release behavior.

Phases 2 and 3: A 160 cc SS 316 vessel (design pressure: 20 bar, design
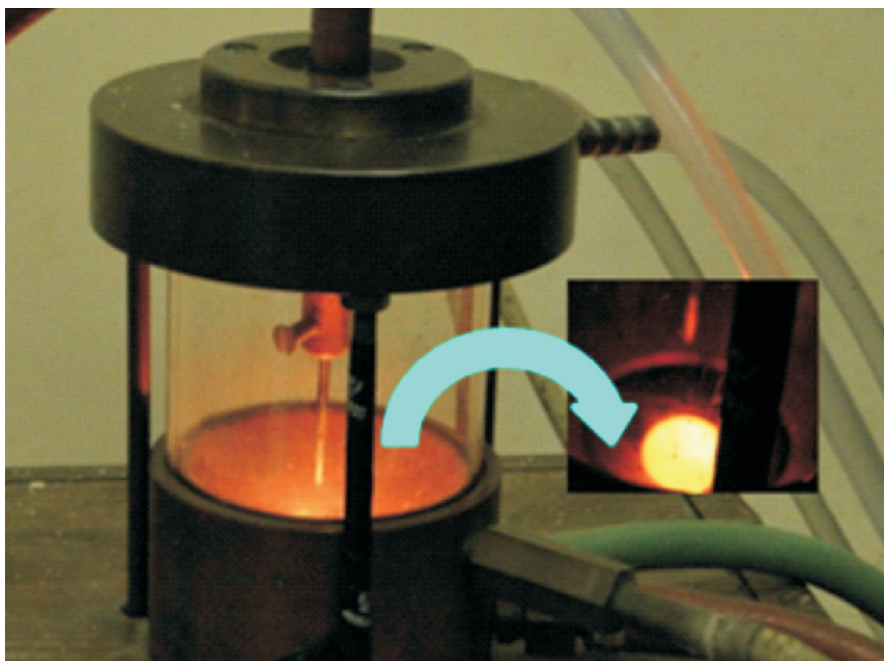
Fig.2: Arc melting furnace used for preparation of the alloy
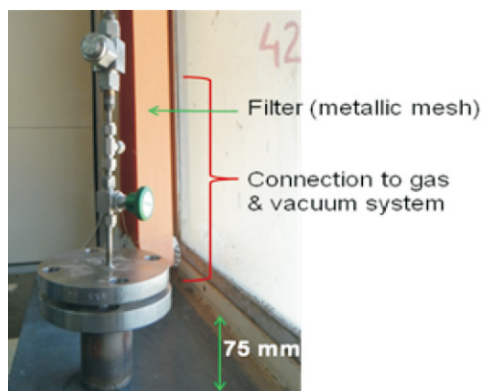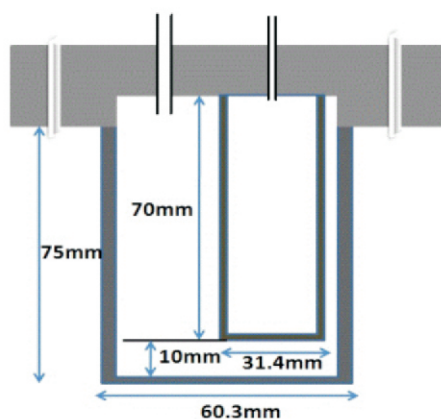
Fig.3: Portable Hydrogen Storage Vessel and its dimensions
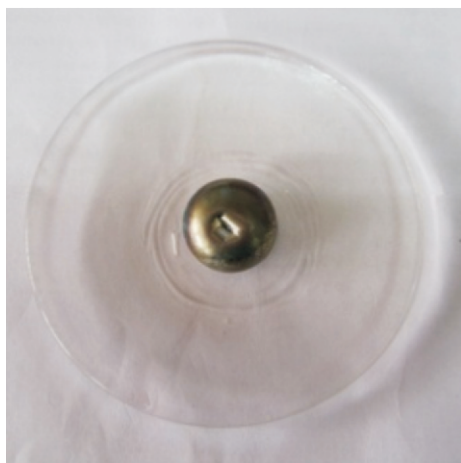
Fig.4: Synthesized alloy (a) 10 gm and (b) 42 gm

temperature: 400°C) was fabricated in-house at Heavy Water Division for housing up to 45 gm Ti-Cr-V hydrogen storage alloy freshly synthesized at Chemistry Division. The vessel is closed with a SS flange using a metallic gasket and the system is fitted with a single inlet/outlet gas line with inline micron filter, leak tight needle valves and toggle valves, as shown in Fig. 3. Provisions for pressure and temperature monitoring have also been made.

For the first set of experiments, about 10 gm of the alloy (photograph of the alloy is shown in Fig 4a) and for the second set, about 42 gm of alloy (photograph of the alloy shown in Fig. 4b) were placed in the vessel. The alloy is capable of storing up to 4 wt.% hydrogen and thus the vessel could store between 4NL and 18 NL of hydrogen gas (i.e. amount of hydrogen generated during one hour operation of 18 NLPH hydrogen generators). Details of the experimental procedure are provided in the next subsection.

Hydrogen storage and retrieval properties of the alloy were tested for 5 cycles each, using commercial grade hydrogen from a cylinder in pulsed mode. For obtaining kinetic data hydrogen storage was done at various flow rates ranging from 5 to 34 NLPH (which is twice the flow rate to be obtained from 18 NLPH hydrogen generator). From the studies it is observed that there is no degradation in the storing capacity of the material. The stable storage capacity observed in all these runs is around 3.8 wt.% hydrogen.

Phase 4: After successful demonstration of hydrogen storage in pulsed and continuous modes using

Ti$_2$CrV, its performance with respect to deuterium was also studied under nearly identical conditions. Representative results comparing alloy behaviour towards hydrogen and deuterium absorption are provided in this report. Simultaneously the long term stability and re-usability of the alloy were also examined.

4) Experimental procedure for hydrogen storage studies

Typical step-wise procedure used during the experimental runs is described below.

a) The storage vessel (Fig 3) was first tested for leak tightness at 1 bar, 5 bar, 10 bar and 15 bar hydrogen pressures. A maximum allowable leak rate of 10^{-6} mbar/s s ensured through Mass Spectrometric Helium Leak Detection (MSLD) technique and the vessel is operated up to 5 bar pressure during the experiments.

b) The freshly prepared alloy buttons (Fig. 4) were manually crushed (Fig. 5), sonicated in ethanol solvent to clean the surfaces and filled into the vessel and its leak tightness is once again established before introduction of hydrogen.

c) The vessel was heated with simultaneous evacuation as per a pre-programmed temperature schedule using electrically heated furnace. Maximum temperature attained during this de-gassing step was about 400°C. Heating was continued for 2-3 hours for complete degassing of the sample, followed by cooling the vessel to room temperature, which takes another 2-3 hours. This step removes surface impurities, adsorbed gases etc. which would otherwise interfere with the alloy's hydrogen uptake ability.

d) Hydrogen storage alloy was studied by introducing commercial grade hydrogen into the vessel in pulses. After saturating the solid with hydrogen, it was again heated to 400°C under dynamic vacuum. This is the surface activation procedure which leads to formation of fine activated powder of the alloy, from irregular shaped chunks.

Fig.5: Crushed alloy button before loading in the reactor
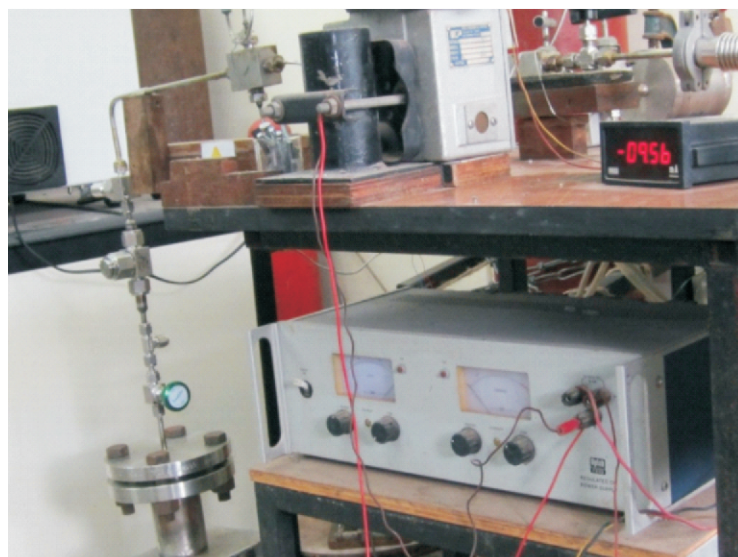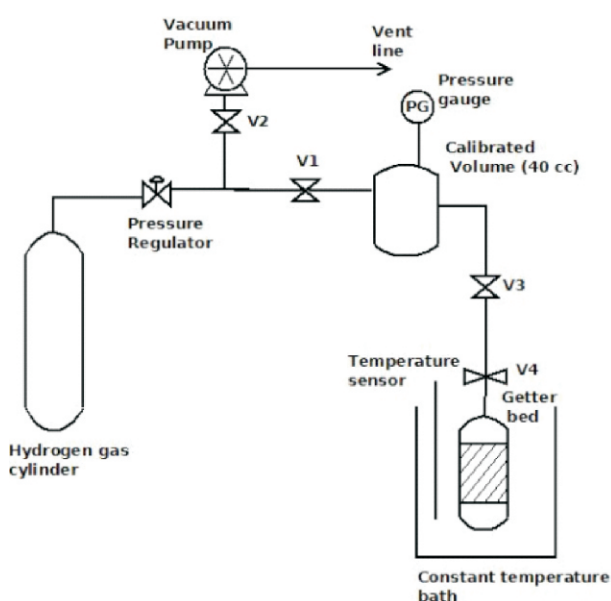
Fig.6: Schematic of hydrogen storage facility (left) along with the actual experimental facility (right)

e) For hydrogen storage run in pulsed mode of operation, the vessel was evacuated at room temperature and placed in a constant temperature water bath. Hydrogen gas from the cylinder was introduced into the loop (Fig. 6) and calibrated the volume by opening valve V1, while keeping V4 and V3 closed. Then V1 was closed (thereby effectively isolating the hydrogen cylinder) and gas was introduced into the evacuated storage vessel by opening V3 and V4. Due to hydrogen absorption by the alloy, pressure drop occurs rapidly. As soon as pressure drops below atmospheric pressure, another pulse of hydrogen was introduced into the vessel. The process was continued till there was no further drop in pressure owing to saturation of hydrogen uptake by the solid. From the total amount of hydrogen introduced till saturation, the hydrogen storage capacity of the alloy is calculated.

f) For hydrogen storage run in semi-batch mode of operation, the storage vessel was evacuated as usual. A desired continuous flow rate of hydrogen into the calibrated volume (and hence the getter bed) was set based on a given pressure rise within the known volume, for certain measured time period. These flow rates were varied in the range of 4 to 34 NLPH. Pressure in the vessel was noted as a function of time at a given constant inflow rate of hydrogen gas. These time-pressure histories were used to establish the kinetics of hydrogen storage by the alloy.
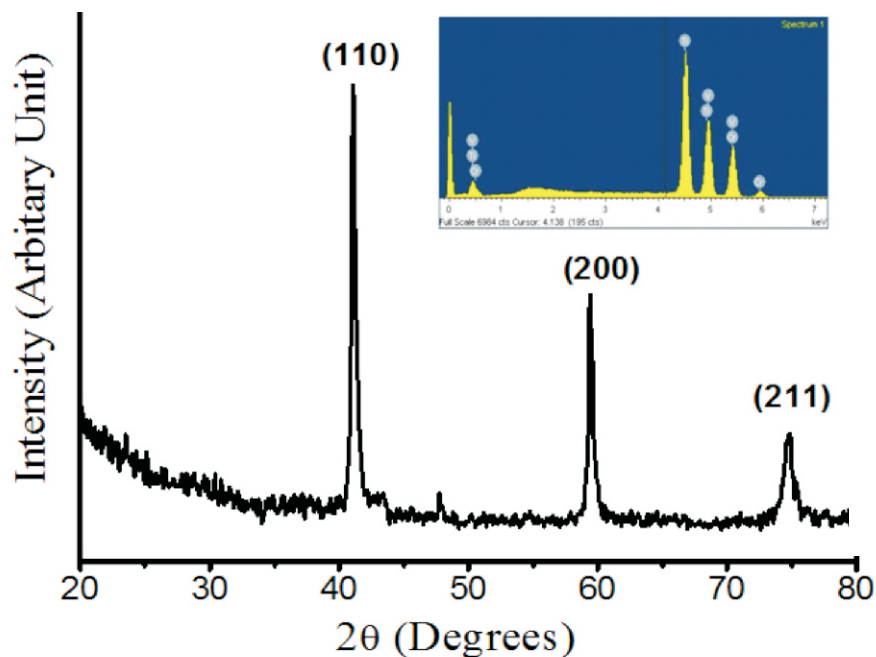
Fig.7:XRD pattern of as prepared Ti$_2$CrV alloy. A representative EDAX profile from the sample is shown as an inset in the same figure

Results

Salient Properties of the Alloy

The developed alloy has been characterized by different techniques

XRD pattern of as prepared Ti$_2$CrV alloy is shown in Fig. 7. It is confirmed from the pattern that Ti$_2$CrV alloy crystallizes in pure body centered cubic (bcc) structure with lattice parameter "a"=3.10Å. To ensure homogeneity in composition of as prepared alloy, EDAX profiles were recorded at various positions on the alloy surface. Average elemental composition of the synthesized material obtained from EDX results matches well with the expected elemental ratio of Ti:Cr:V = 2:1:1. Back scattered electron (BSE) image of Ti$_2$CrV also confirms formation of compositionally homogeneous alloy without any phase separation.

Observations during hydrogen storage studies

Major observations made during hydrogen storage runs, both in pulsed mode and in semi-batch mode are listed below:

- The total hydrogen storage capacity of the alloy stabilizes at about 3.8 wt% hydrogen after 2-3 cycles of hydriding and dehydriding.

- Hydrogen absorption takes place quite rapidly at sub-atmospheric pressure (about 0.2-0.5 bar) at room temperature for freshly activated alloy. Uptake rate decreases as the alloy gradually become saturated with hydrogen. Pressure composition isotherm of Ti$_2$CrV alloy at room temperature shows the amount of hydrogen it can store reversibly within the studied pressure range at room temperature. In Fig. 8, the equilibrium hydrogen pressure is plotted against the number of hydrogen atoms stored per formula unit of the alloy (H/Formula Unit). From the study it is found that the
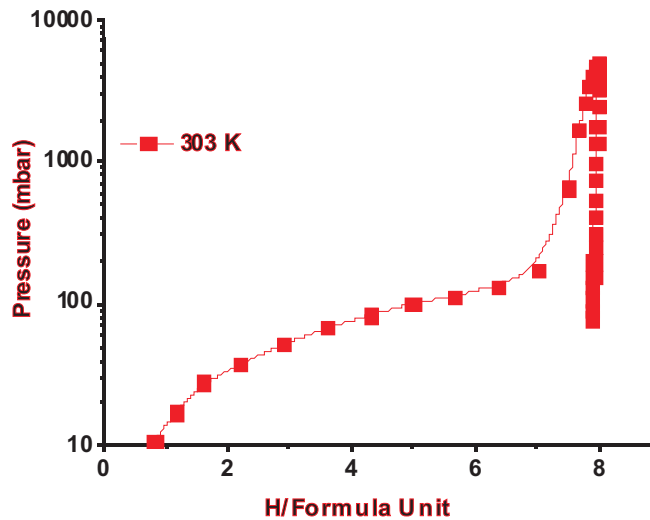
Fig.8: Hydrogen absorption desorption at room temperature as a function of pressure for Ti$_2$CrV alloy
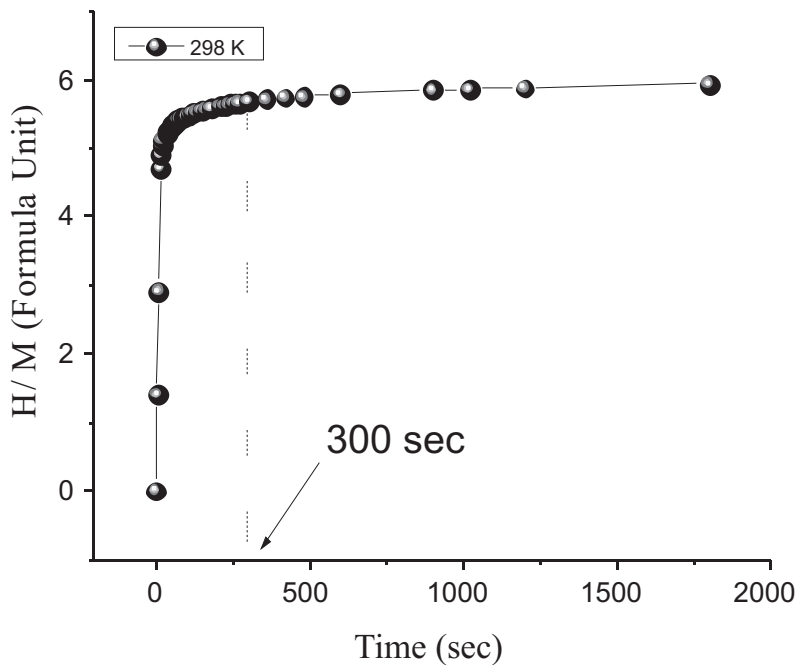
Fig.9: Hydrogen absorption kinetics of Ti$_2$CrV alloy at room temperature
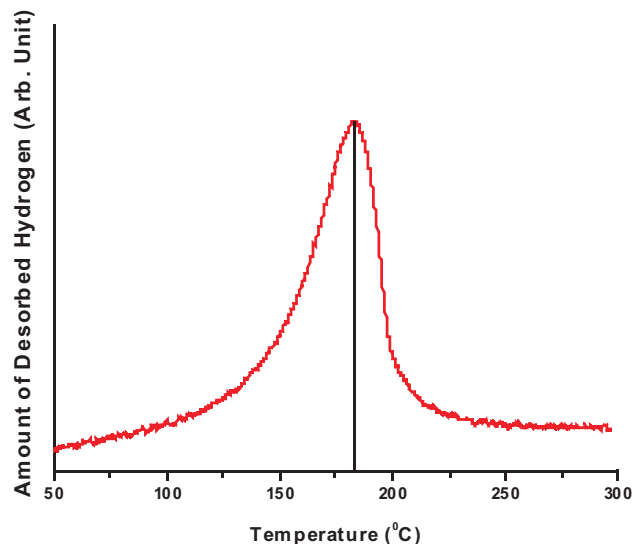
Fig.10: In situ hydrogen desorption profile of Ti$_2$CrV alloy

alloy can store ~8.9 H/formula unit which corresponds to 3.9 wt% of hydrogen. From the PCT profiles at different temperatures enthalpy of hydrogenation of the alloy has been evaluated and found to be -64.4 kJ/mol H$_2$.

- The rate of hydrogen absorption by Ti$_2$CrV alloy is recorded after one hydrogen absorption -desorption cycle. Fig. 9 shows the room temperature kinetics of hydrogen absorption under isothermal condition. From the figure it is clear that the alloy absorbs hydrogen without any incubation period and it reaches near saturation value within 5 minutes.

- Temperature programmed desorption experiment has been performed in-situ without exposing the sample in air atmosphere to understand the desorption behavior. The hydrogen desorption curve is characterized by a clear single peak at about 180 °C (Fig. 10) with initiation of desorption process at ~100 °C.

- The alloy can be activated in one cycle. Fine micron sized alloy powder (10-15 micron) is generated during this step which is extremely useful for rapid hydriding and dehydriding of the alloy. SEM micrograph shown in Fig. 11 suggests that most of the alloy particles have size in the range of 100-200 μm and particle sizes are found to decrease after hydrogenation.

- Depending on the amount of the alloy and rate of hydriding, there is about 3-4 °C increase in the temperature in the storage system during the hydriding process.
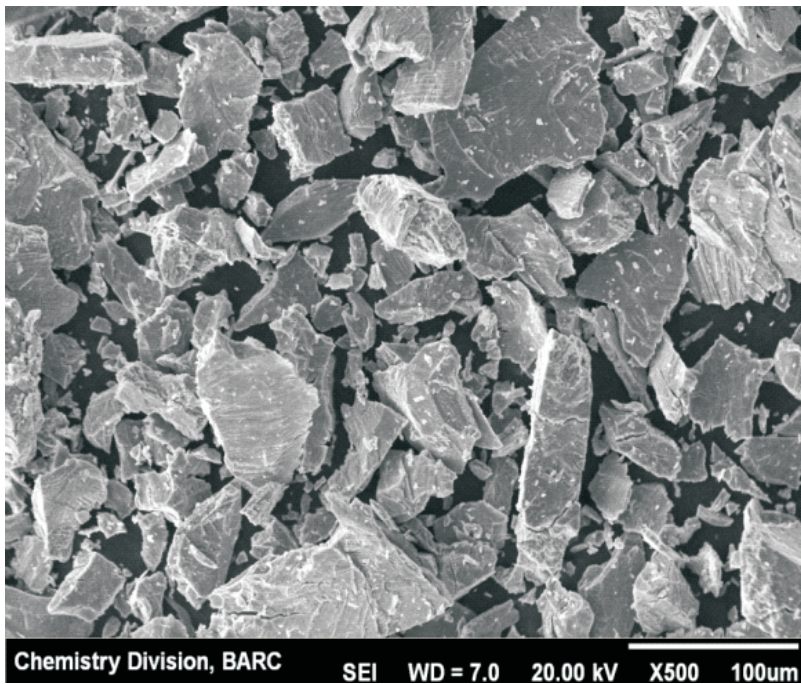
Fig.11:SEM micrograph of Ti₂CrV hydride

Table 3. Volume of hydrogen absorbed by the material as a function of flow rate and time for 11 g of material

Sr. No.	Flow rate (ml/min)	Time (minutes)	Volume absorbed (ml)
1	26.5	30	795
2	53	30	1590
3	44	90	3960

Table 4. Volume of hydrogen absorbed by the material as a function of flow rate and time for 42 g of material

Sr. No.	Flow rate (litre/hr)	Time (minutes)	Volume of hydrogen (litre)
1	5	180	15
2	9	110	16.5
3	18	59	17.7
4	34	32	18.1

During runs with deuterium gas, a similar trend has been observed indicating very little isotope effect with respect to thermodynamics of hydrogen/deuterium absorption by the material.

• Hydrogen storage data for 11 g and 42 gm material in the continuous mode is described below and presented in Table 3 and 4, respectively.

(In all the cases instantaneous hydrogen absorption is achieved without any hydrogen pressure build up and hydrogen uptake is found to be ~ 95 % of the expected value. Hydrogen desorption initiate at ~ 100 °C and with heating hydrogen pressure builds up).

• There is no appreciable loss of alloy material during evacuation and hydrogen absorption desorption study and the entire batch of solid kept in the test vessel could be recovered. This is confirmed by weighing the alloy powder left in the vessel after some cycles of testing.

It is observed that uptake and release of deuterium gas by the alloy are qualitatively similar, though there are some differences in the rates of hydriding, which is one of the expected features of the isotope effects in solid state hydrogen storage. The alloy shows maximum deuterium uptake ~ D/M = 9 at room temperature under a deuterium pressure of 15 bar which is similar to its hydrogen uptake. Like hydrogenation, deuteration also leads to phase change from BCC to FCC and the corresponding XRD patterns of hydrides and deuterides are shown in Fig. 12.

Desorption studies were performed on surface poisoned hydride and deuteride using differential scanning calorimetric (DSC) experiments at 10°C/min. temperature ramp under flowing argon atmosphere. DSC studies show that desorption of Ti₂CrV deuteride peaks is quite close to its hydride desorption temperature indicating similar stabilities of both hydride and deuteride of Ti₂CrV alloy.

Hydrogen isotope effect can be explained as an interplay of two important thermodynamic parameters namely, enthalpy and entropy.
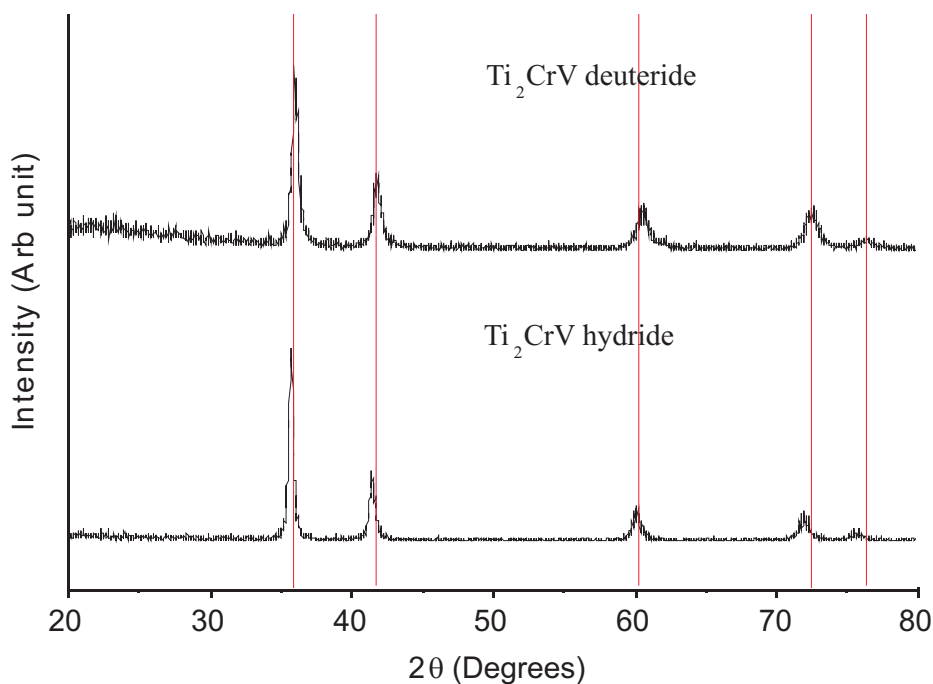
Fig.12: XRD patterns of hydride and deuteride of Ti₂CrV alloy

these systems arise mainly due to differences in associated entropy change values upon dehydrogenation or de-deuteration. Since the entropy of de-deuteration is higher compared to that of dehydrogenation, a normal isotope effect is expected for this alloy.

- It is found that fine alloy powders when exposed to air lose their hydrogen storage capability within a day or less. The freshly prepared alloy buttons of larger size do not suffer from this problem and they can be stored without additional precautions in typical glass and plastic sample holders.

- The alloy is found to retain its hydrogen storage capacity over 1 year period when stored in saturated condition under H_2 atmosphere (2-4 bar (absolute)). The alloy sample aged for 1 year in this manner was found to show ~95% of its initial max. H_2 storage capacity.

Enthalpy is the controlling factor for the relative stabilities of the corresponding protide/deuteride /tritide. Desorption temperature gives an idea about the stability of isotope hydrides thus indirectly tells about their enthalpy variation. From the desorption studies it is found that the stability of hydride and deuteride of Ti₂CrV alloy is same indicating that the enthalpy of dehydrogenation/de-deuteration will not influence the isotope effect for Ti₂CrV-H_2/D_2 systems. Hence, the isotope effects in

Fig.13: Variation of Hydrogen and Deuterium gas for establishing isotope effects

Major lessons and accomplishments

The major findings and positive outcomes from the joint exercise may be summarized as follows:

- Traditional rare earth based hydrogen storage alloys, which are commercially available, have low storage density of about 1.5 wt% hydrogen. Moreover they need high hydrogen pressure (about 15 to 20 bar) for the loading step. There is also a possibility of high quality rare earth supply related constraints for large scale alloy synthesis since the rare earths are available only at very few locations worldwide and purification process for getting pure rare earth metals is really difficult. The developed Ti based alloy (Ti_2CrV) does not have any rare earth constituents and it absorbs hydrogen even at sub-atmospheric pressure with relatively larger storage capacity. Thus the use of this alloy resolves several technical challenges arising from the use of more conventional storage materials. In-house developed H_2 storage alloy shows higher storage capacity (3.8 wt %), re-usability and resistance to oxidation compared to commercially available rare earth alloy (1.5 wt %) and other materials for hydrogen isotope storage (e.g. U: 1.25 wt %). It can absorb hydrogen at room temperature and sub-atmospheric pressure, which is extremely helpful for room temperature in-situ hydrogen storage.

- Traditional alloys require 5 to 10 cycles of activation before it demonstrate reliable and reproducible hydrogen uptake and release characteristics. The Ti_2CrV become activated within 1-2 cycles itself and is therefore an improvement over conventional materials.

- The alloy has been found to retain up to 95% of its maximum storage capacity after a gap of over one year when kept under hydrogen overpressure, thereby exhibiting shelf stable characteristics, which is a desirable property of these storage materials.

- Reduction in storage vessel weight and overall dimensions through successive design changes have been accomplished as greater confidence has been gained in operating these systems.

- The alloy has been found to be suitable for storage of hydrogen isotopes as well owing to its favourable thermodynamic and kinetic behaviour.

Future plans and the way forward

The alloy Ti₂CrV has been determined to be a very promising hydrogen storage material and is expected to play an important role in DAE's hydrogen generation and storage program. It has potential to be commercialised as a sustainable substitute for the present day rare earth based solid state hydrogen storage systems. The activities planned for the future, using Ti₂CrV alloy for hydrogen storage are as follows:

a) Development of process for bulk synthesis of the alloy for storing 144 l hydrogen (18NLPH generator for 8 hrs): Technology transfer to private industry may be an option for this.

b) Development of fully welded standardized module for hydrogen storage: Standard modules similar to commercially available rare earth based hydrogen storage modules of different capacities may be developed as per user requirements. There are many other applications which may be explored with this material.

*Corresponding author

Dr. (Smt.) Seemita Banerjee

References

1. Materials for hydrogen storage: Current research trends and perspectives, Annemieke W. C. van den Berg and Carlos Otero Arean, Chem. Commun., 6 (2008) 668–681.

2. Hydrogen-storage materials for mobile applications, Louis Schlapbach & Andreas Züttel, Nature, 414, (2001) 353-358.

3. Effect of cycling on hydrogen storage properties of Ti₂CrV alloy, A Kumar, K Shashikala, S Banerjee, J Nuwad, P Das, CGS Pillai, Int. J. Hydrogen Energy, 37 (2012) 3677-3682.

4. Hydrogen storage properties of Ti2- xCrVMx (M= Fe, Co, Ni) alloys, A Kumar, S Banerjee, CGS Pillai, SR Bharadwaj, Int. J. Hydrogen Energy, 38 (30), 13335-13342.

5. Synergic effect of vanadium trichloride on the reversible hydrogen storage performance of Mg-MgH₂ system, S Kumar, P K Singh, GVSN Rao, Y Kojima, V Kain, Int J Hydrogen Energy 43 (32), (2018) 15330-15337.

6. Influence of Laves phase on microstructure and hydrogen storage properties of Ti–Cr–V based alloy, S Banerjee, A Kumar, P Ruz, P Sengupta, International Journal of Hydrogen Energy 41 (2016) 18130-18140.

7. First-principles study of the interaction with transition metal (Ti, V, Ni) doped Mg(0001) surface: Implications for H-storage materials, S Banerjee, CGS Pillai, C Majumder, J. of Chem. Phys., 129 (17) (2008) 174703.

8. Effect of surface functional groups on hydrogen adsorption properties of Pd dispersed reduced graphene oxide, TK Das, S Banerjee, M andey, B Vishwanadh, R J Kshirsagar, V Sudarsan, Int J Hydrogen Energy, 42 (12), 8032-8041.

9. Nature of the Pd–CNT interaction in Pd nanoparticles dispersed on multi-walled carbon nanotubes and its implications in hydrogen storage properties, T Das, S Banerjee, K Dasgupta, J B Joshi, V Sudarsan, RSC Advances 5 (52), 41468-41474.

10. Nitrogen doped porous carbon derived from EDTA: Effect of pores on hydrogen storage properties, TK Das, S Banerjee, P Sharma, V Sudarsan, PU Sastry, Int J Hydrogen Energy, 43 (17), 8385-8394

11. Synthesis of cobalt hexacyanoferrate nanoparticles and its hydrogen storage properties, A Kumar, AB Kanagare, S Banerjee, P Kumar, M Kumar, V Sudarsan, Int J Hydrogen Energy, 43 (16), 7998-8006, 2018.

12. Alkali-metal-induced enhancement of hydrogen adsorption in C60 fullerene: an ab initio study KRS Chandrakumar, S K Ghosh, Nano letters 8 (1), 13-19, 327, (2008).

13. Computational Investigation of Hydrogen Adsorption by Alkali Metal Doped Organic Molecules: Role of Aromaticity, K Srinivasu, KRS Chandrakumar, S K Ghosh, Chem Phys Chem 10 (2), 427-435 (2009).

14. High capacity reversible hydrogen storage by metallo-carbohedrenes: An ab initio molecular dynamics simulation study, S Banerjee, CGS Pillai, C Majumder, Applied Physics Letters 102 (7), 073901, (2013).

15. Pd-Ag-Cu dense metallic membrane for hydrogen isotope purification and recovery at low pressures, Subhasis Pati, Ram Avtar Jat, N. S. Anand, D. Joyson Deros, K. N. Karn, S. K. Mukerjee, S. C. Parida, Journal of Membrane Science, Volume 522, 15 January 2017, Pages 151-158.

16. Hydrogen Isotope Effect on Thermodynamic and Kinetics of Hydrogen/Deuterium Absorption–Desorption in Pd0.77Ag0.10Cu0.13 Alloy, Subhasis Pati, Ram A. Jat, Sapan K. Mukerjee, and Suresh C. Parida, J. Phys. Chem. C 2015, 119, 19, 10314–10320.

17. Simulation studies of the characteristics of a cryogenic distillation column for hydrogen isotope separation, R Bhattacharyya, K Bhanja, S Mohan, Int J Hydrogen Energy, 41 (9), 5003-5018 (2016).

18. Solid state storage of hydrogen and its isotopes: An engineering overview, Renewable and Sustainable Energy Reviews, 41(2015) 872-883.

Fiber Optic Interferometer Sensor for Vibration Sensing Applications

Anisha Acharya, Nitin Kawade*

Laser and Plasma Technology Division

Abstract

Predictive Maintenance and condition monitoring of machines are very crucial aspects for any industry. This article discusses a Fiber Optic Fabry Perot Interferometer (FPI) based dynamic displacement sensor developed in BARC for vibration sensing applications. The sensor is designed to measure precise vibration remotely by making use of a fiber optic probe. The use of silica based fiber optics and remote electronics makes the sensor suitable for measurements in radiation environment. The sensor probe is demonstrated to measure dynamic displacements at a working distance of 5 cm with an amplitude resolution of 12 nm, a precision of 1.4 nm and a standard deviation of 2%. The sensor is also able to measure multi-frequency vibrations and computes vibration spectrum with frequency identification in the range of 0-1 kHz. The sensor was tested with known source of vibrations generated using standard piezo-actuators. The results obtained for vibration measurements of a hard disk are also presented. This confirms usability of the sensor in various non-contact vibration sensing applications mainly in high radiation and EMI/EMC prone environments.

Keywords: Vibration Sensing, Fabry-Perot Interferometer, Piezo-Actuators

Introduction

Vibration Sensing is very important for predictive maintenance and condition monitoring applications. Parameters generally measured for such applications include displacement, velocity, and acceleration. For cases where strain or misalignment measurements are necessary, displacement is measured. To determine fatigue, measurement of velocity of vibrating parts is helpful for analysis. To carry out impact and force analysis, acceleration (in g) is typically measured. Acceptable vibration levels vary for different machineries i.e. for e.g. in a precision machining tool the acceptable vibration is <1mm/s while a vibration level of 4 mm/s is considered to be acceptable for typical industrial machineries[1]. Early diagnosis and vibration profile analysis prevents fatal failures and reduces down time in industries.

In a nuclear industry, a critical activity at a nuclear power plant involves monitoring the condition of the equipment, looking for early warning signs and identifying abnormalities [2]. The equipment generally include compressors, cooling tower gearboxes, generators, motors, pumps, and turbines. Another critical parameter in a nuclear power plant that requires monitoring is flow induced vibrations. Flow-induced vibrations are driven by highly energized flow which induces vibrations in relatively flexible structures. In nuclear reactors, flow-induced vibrations are mostly created by reactor coolant impinging on flexible reactor internals, fuel rods, shielding, or heat exchanger tubes [3].

Hence for all predictive maintenance purposes, online vibration monitoring is necessary. Generally, accelerometers are employed in all nuclear installations. However recently, fiber optic sensors are being considered as potential replacements in the nuclear power industry. Fiber optic sensing technology offers performance enhancements over conventional systems in terms of dynamic range, sensitivity, signal isolation, distributed measurement, and compactness. The electronic components of a fiber optic sensing system may be located remotely, allowing installation of the sensing element in electrically noisy, chemically hazardous, high temperature, radiation or potentially explosive process measurement environments[4].

Many fiber optic techniques are reported in literature such as self-referenced techniques[5][6], white light interrogation technique[7], specklegram and image processing-

based technique[8]. The sensor developed works on the principle of laser interferometry which has advantages of easy alignment, larger standoff distance, measurement displacement range extending to micrometres and nanometres, exceptional sensitivity, and high resolution.

So far, however, interferometry was exclusively used in calibration processes due to its high costs[9][10]. The use of a fiber-optic FPI operating at telecom wavelength enables miniaturization and cost reduction of the interferometer. To further reduce the cost of the sensor, frequency modulation phase generated carrier technique for the interferometry is employed. In this technique, the requirement of expensive fiber optic components is minimal hence reducing the overall cost of the sensor without compromising on the performance of the sensor.

Working Principle

An FPI consists of two parallel flat semi-transparent reflectors separated by a fixed distance. This arrangement is called as etalon. Reflectors can be mirrors, interface of two dielectrics, fiber tips or fiber Bragg gratings. Monochromatic light when incident on one of the mirrors at a certain angle will undergo multiple reflections within the cavity and produces an interference pattern. The spatial and temporal characteristic of the interference pattern varies according to the wavelength of incident light, etalon length, reflectivity of reflectors and refractive index of the etalon.

An FPI based displacement sensor will be hence sensitive to change in etalon length if all other parameters

are kept constant. In such sensor, etalon is created between the fiber tip of the sensor and an external reflective vibrating target i.e. the interferometer is set in an extrinsic configuration. A time varying interference pattern is generated as a result of target vibration which modifies the etalon length. For a low-finesse FPI [11], intensity variation as a result of the target vibration can be expressed as:

$$I = I_1 + I_2 + 2\sqrt{I_1 I_2}\cos\left(\frac{4\pi nx}{\lambda} + \varphi_o\right) \qquad (1)$$

where, I_1 and I_2 are the intensities of light reflected from sensor head and external target respectively, n is the refractive index of the etalon (air for extrinsic FPI), x is the displacement of the vibrating target, λ is the wavelength of laser, φ_o is the phase offset due to ambient temperature fluctuations and initial cavity length.

For smaller displacements, the position of the remote target is inferred by calibrating the detector signal along the maximum slope of the interference pattern. For larger displacements, quadrature detection methods are used to recover phase change of interference pattern with constant sensitivity [10]. One of the techniques to retrieve quadrature signals is Frequency Modulated Phase Generated Carrier (FMPGC) method [11] wherein emission frequency of the laser is modulated. In this method, the detector signal would require signal processing operations to retrieve quadrature signals. Displacement/vibration of the target can be then obtained by demodulating the phase of the quadrature signals.

In the instrument, the sensor employed

is an FPI with a double pass sensor head [9]. The sensitivity achieved for such configuration is double of that obtained in a typical FPI sensor. The phase variation due to vibration of a target with sinusoidal excitation is expressed as[10]:

$$\varphi_x(t) = 2 \times \frac{4\pi n}{\lambda} a \cos(\omega t) \qquad (2)$$

where a is the amplitude of vibration in μm and ω is frequency of excitation in rad/s. The direction ambiguity is resolved by using FM-PGC method [12][8] and the phase is demodulated to obtain vibration.

Instrument design

The designed instrument comprises of an optical and an electronics hardware as well as a signal processing software. The hardware includes fiber optics, optoelectronics and an analog In-phase/Quadrature (I/Q) generator. The software executes the demodulation algorithm on the quadrature signals and processes the signal to derive vibration parameters like displacement, velocity and, acceleration.

Sensor Hardware

The sensor was designed with a modulated Distributed Feedback (DFB) laser to generate carrier phase. The laser chosen is a 2 mW pigtailed laser diode in a butterfly package with a center wavelength of 1541.86 nm and linewidth < 4pm. Narrow linewidth, compact packaging and a pigtail configuration makes this laser suitable for fiber optic interferometry applications. The laser injection current is modulated at a bias current of 37 mA ± 1.28 mA with a sinusoidal frequency of 113 kHz. The average
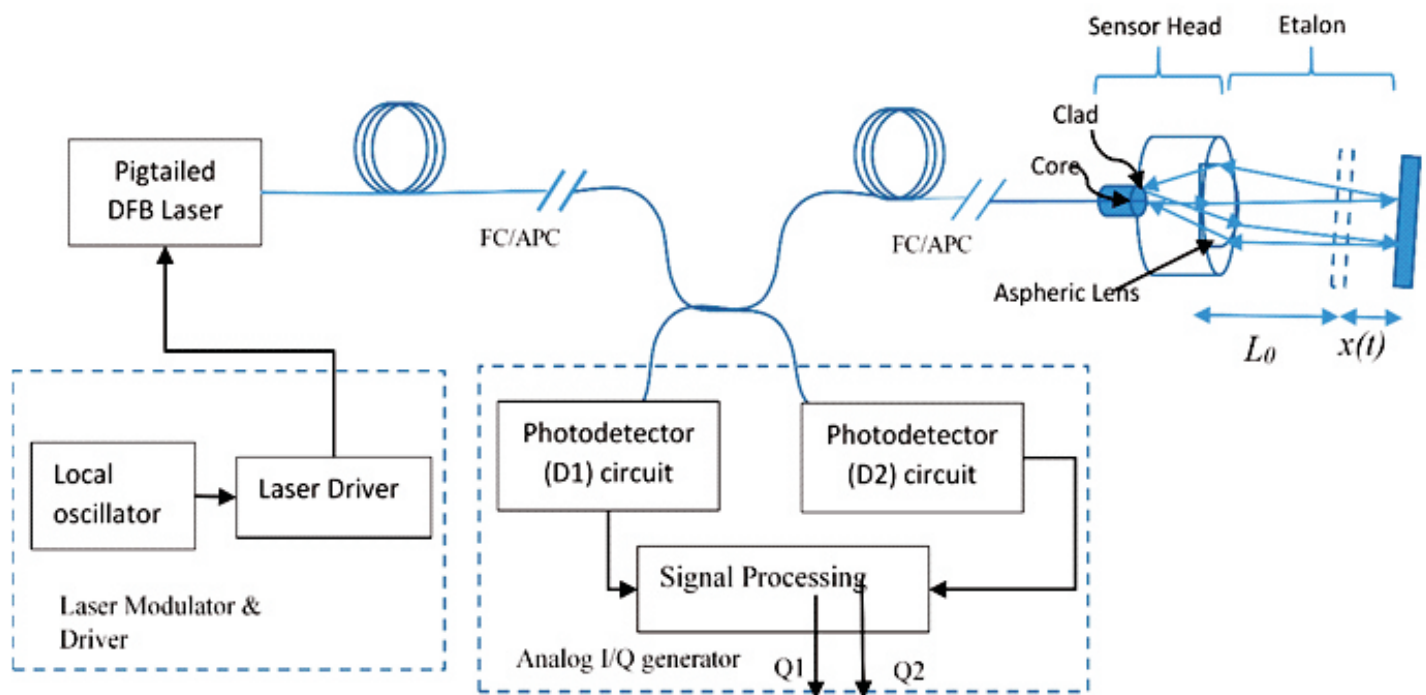
Fig.1. Block Diagram of the Sensor

wavelength change per mA current (dλ/dI) was found to be 5.1 pm/mA under DC operating conditions. Thus, the laser output generates required emission frequency modulation for the interferometer. The drift of laser power with time without any temperature compensation was also monitored and was found to be 41 µW.

An active Colpitts oscillator was designed and used for modulation. Laser was coupled to a 1m long probe with sensing head via a 3dB fiber optic bidirectional coupler. All the fiber optics in the sensor unit including the probe were SMF 28e fibers, a commercial telecommunication grade fiber with attenuation < 0.18dB/km at 1550 nm with a core/clad dimension of 9 µm / 125 µm. An extrinsic configuration of FPI is used wherein the etalon is formed between the fiber optic probe/sensor tip and an external reflective target object at one end of the 3 dB coupler (Fig.1)[10]. All the fiber optic components are interconnected using FC/APC

connectors. This lowers the coupling loss and prevents back reflections in the interconnections. An aspheric collimator is used in the sensor head to obtain a folded cavity.[9] The spot size of the collimated IR beam was 1.375mm FWHM. The spot size was measured by imaging and processing the fluorescence created by the collimated IR beam. A time varying intensity pattern generated as a result of target vibration was detected at photodiode D1. An additional photodetector D2 was used to detect

laser power modulation and remove LIM (Light Intensity Modulation) in the system. The photodetectors used in the system are high bandwidth InGaAs Photodiodes with FC adapters with an active area diameter of 150 µm.

An Analog I/Q (In-phase/Quadrature phase) generator was designed to perform light intensity compensation (LIC), carrier mixing, and filtering operations [10] as shown in the block diagram (Fig. 2). The figure shows the
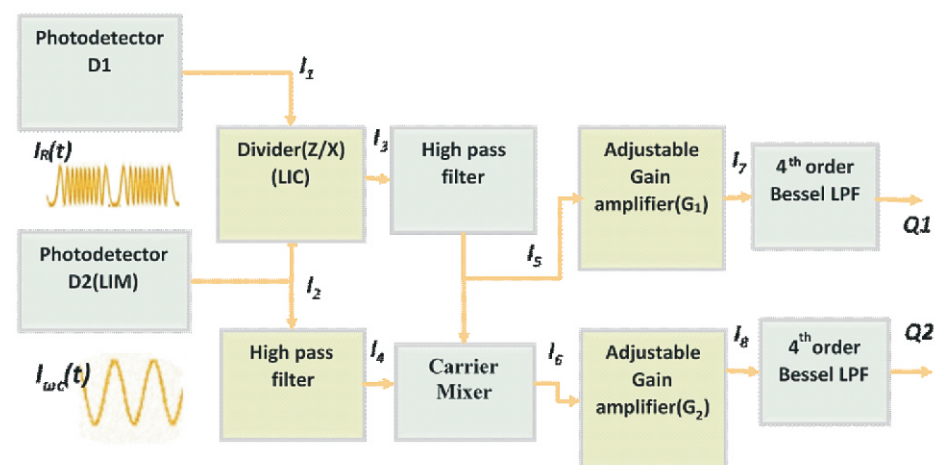
Fig.2. Diagram of the Analog I/Q generator
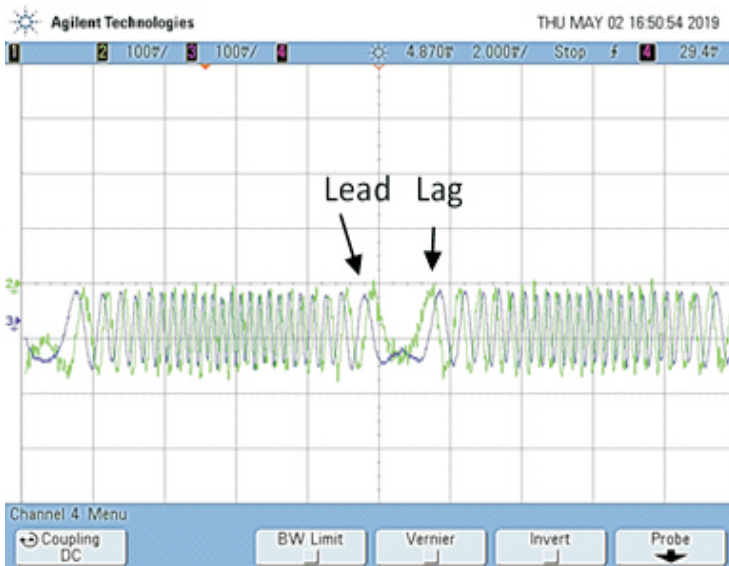
Fig.3. Quadrature Signals (Q1 and Q2)
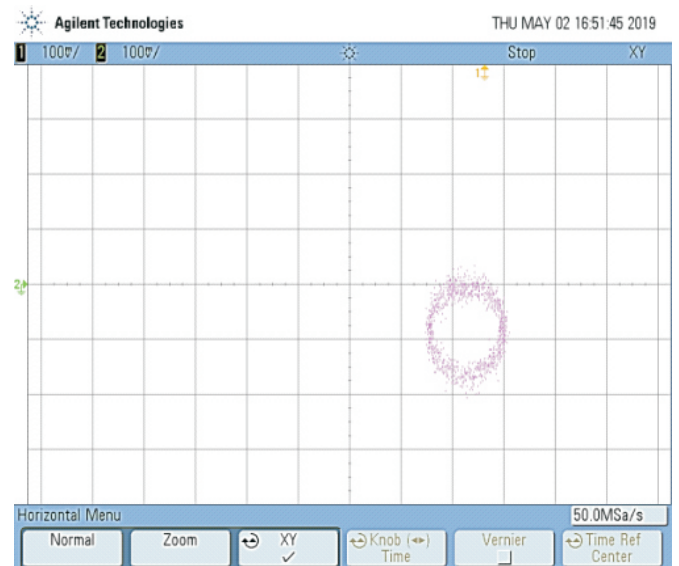
Fig.4. Lissajous Pattern
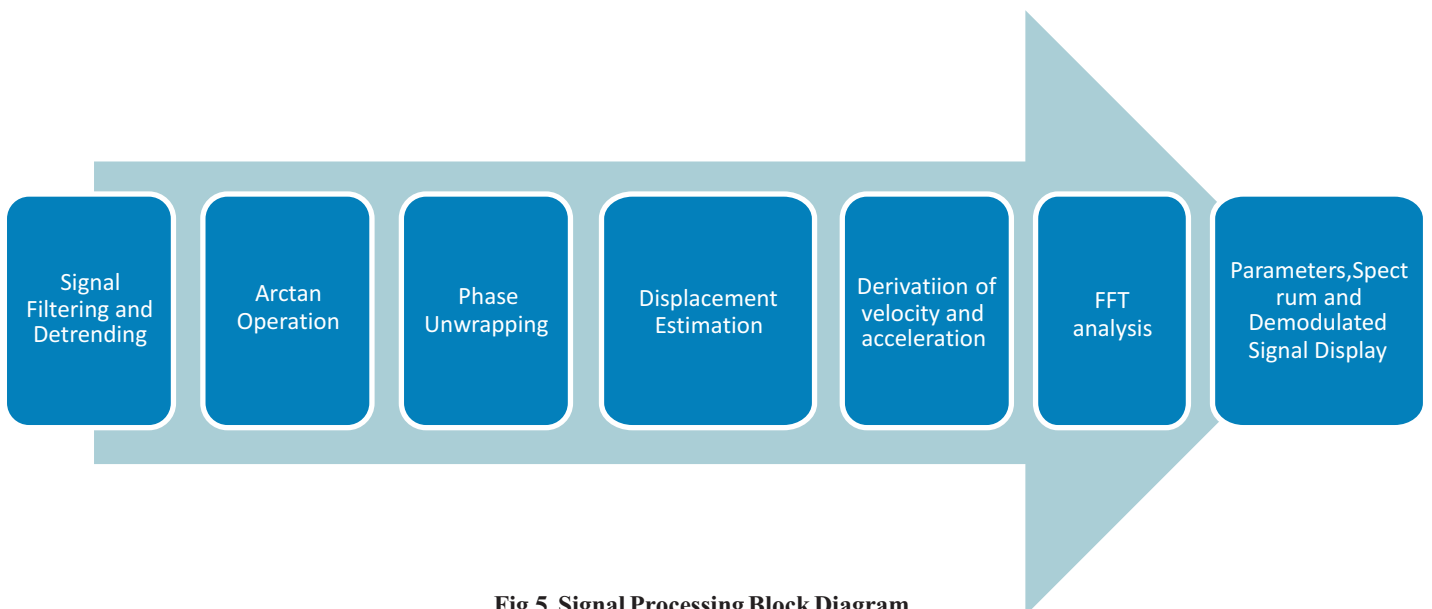
Fig.5. Signal Processing Block Diagram

process signals in the analog hardware. Carrier mixing and filtering yield quadrature signals (Q1 and Q2)) which are 90 degrees out of phase.

The quadrature signals obtained in the setup are shown in Fig.3. The signals Q1 and Q2 are out of phase by 90 degrees and this is evident from the lead lag relationship indicated. The quadrature condition was confirmed by observing the Lissajous figure (Fig. 4) recorded in an oscilloscope.

Software

The quadrature signals obtained (Fig. 3) were digitized by an 8 bit PCI

based Analog to Digital Converter at a maximum sampling frequency 131 kS/s with a voltage range of ±0.5V [10]. Arctangent algorithm and phase unwrapping algorithms were implemented to obtain dynamic displacement from the quadrature signals. For signal analysis, FFT spectrum of the measured displacement was displayed on a Graphical User Interface (GUI) created using MFC libraries. Parameters such as velocity and acceleration were also derived from the measured displacement and displayed on the GUI in a real-time

environment. A block diagram of the signal processing module is shown in Fig.5

Testing and Characterization

i). **Performance Parameters**

Dynamic displacement of a piezo actuator with a stroke length of 9 μm (150/7/7 VS 12) was measured for different range of displacement and frequencies. A mirror of 68% reflectivity was used on the piezo actuator to provide a reflective surface (Refer Fig.6). Repeatability in measurements with change in ambient conditions was also observed.
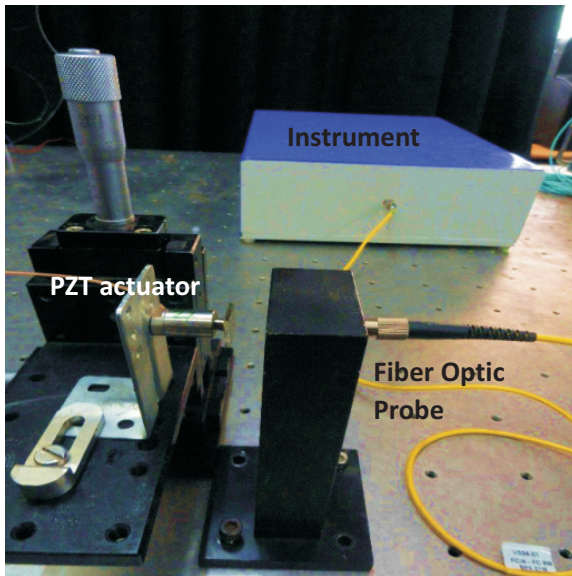
Fig.6. Experimental Setup
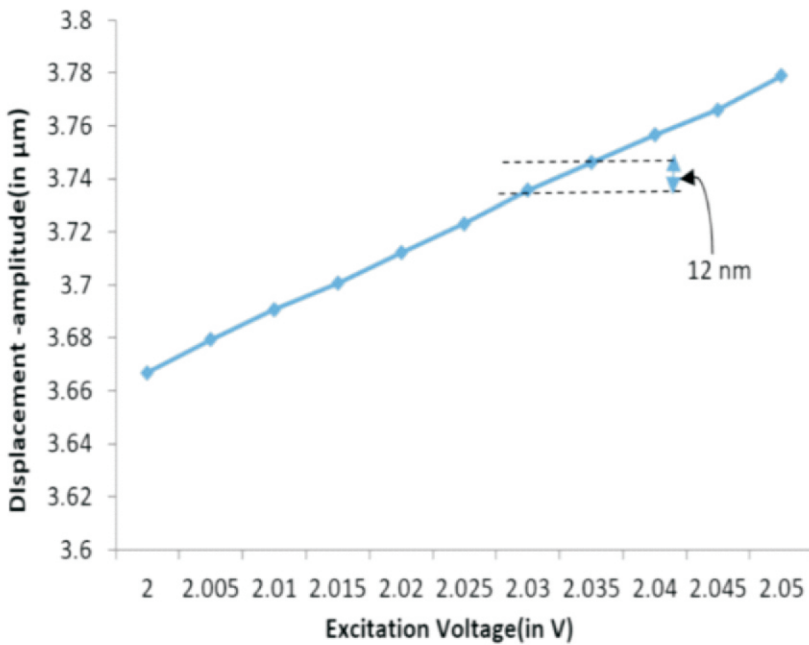
Fig.7. Excitation Voltage vs Displacement
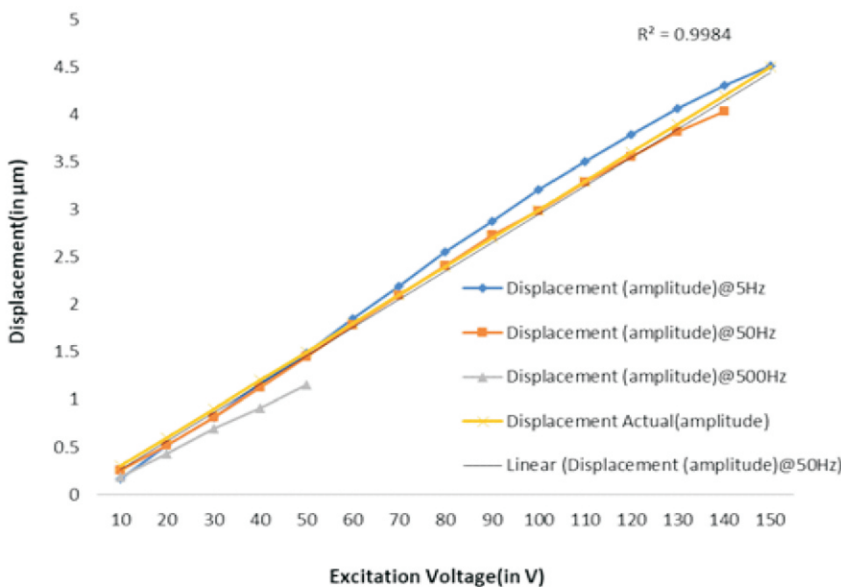
Fig.8. Response of PZT actuator measured using the sensor

The standard deviation in the measurement for a single frequency excitation was found to be 2%. The resolution of the sensor was measured by varying the input at the signal generator from 2 V to 2.05 V with a step change of 0.005 V at a frequency of 5 Hz. The sensor was able to resolve displacement of amplitude 12 nm (refer Fig. 7) with a precision of 1.4 nm.

To check the linearity of the sensor, the piezo actuator was given excitations ranging from 10V to 150V which corresponds to ideal displacement of amplitude 0.3µm to 4.5µm. The readings were taken for three different frequencies i.e. 5 Hz, 50 Hz and 500 Hz. The graph of the displacement estimated is shown in Fig.8. It is found that R2 value for linear fitting for 50Hz excitation is 0.9984. Hence, it was confirmed that the sensor has a good linear response.

ii) Response to Multi-Frequency Excitations

The response of the sensor to multiple frequencies of vibration was measured by subjecting the PZT to a combination of two or more frequencies. Various frequency combinations were taken into account over a frequency range of the sensor. The sensor's response to a beat frequency excitation is shown in Fig 9. As one can observe in the spectrum, both the frequencies are detected. The amplitude of 50Hz signal is greater than that of 52Hz by 56nm because of response of the PZT. The frequency resolution of the sensor is 1Hz hence the two peaks in the FFT spectra are clearly visible.

Another vibration profile that was measured comprised of an excitation
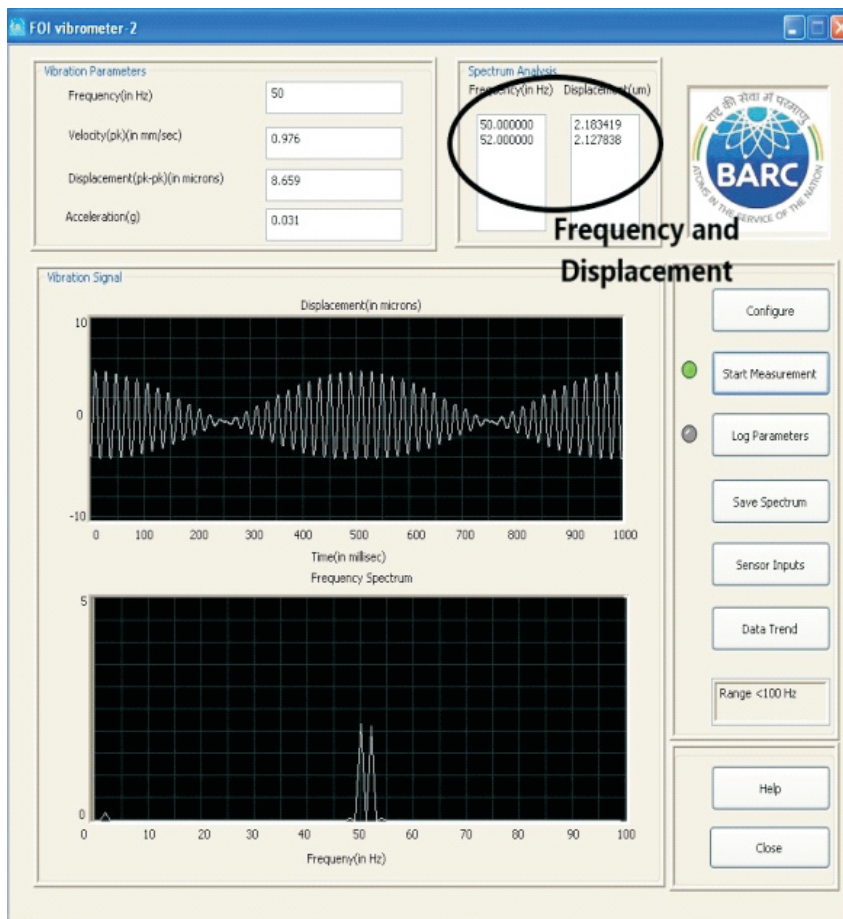
Fig.9. Spectrum of beat frequency Vibration
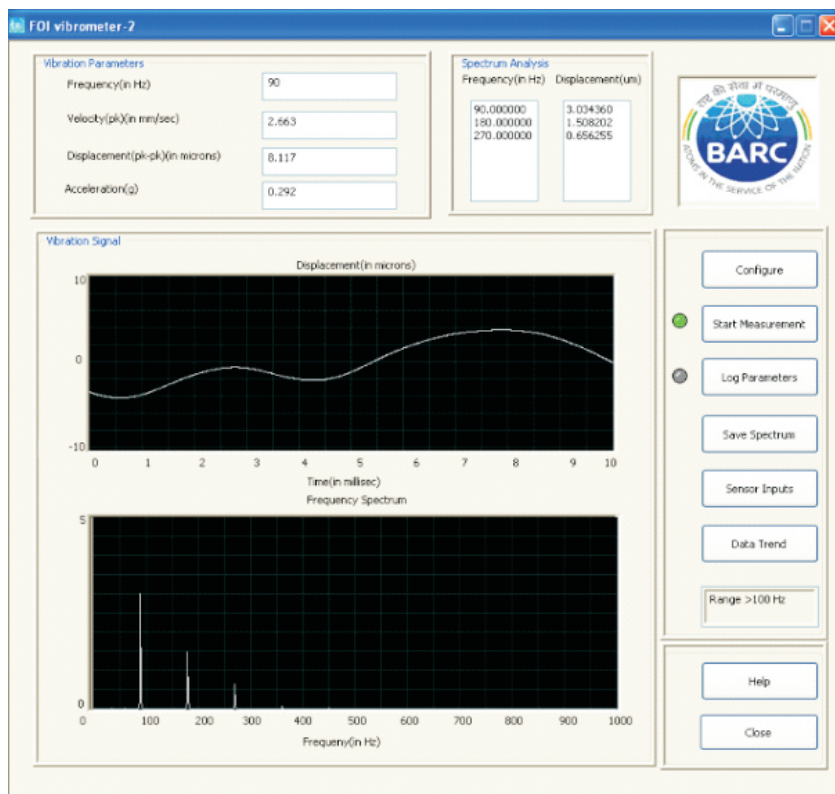
Fig.10. Spectrum of Hard-disk Wobble

signal with frequency of 2Hz and 500Hz. These signals are typically expected in machineries comprising of rotating parts with high rpm. There also exists slow drift and offsets due to static misalignment in such cases which contribute to low frequency displacement. In the experiment conducted, both the frequencies were detected. Owing to the high frequency component i.e. 500Hz, there was also a considerable acceleration of 0.764g pk.

iii) Measurement of Hard-disk Wobble

To detect wobble in mechanical systems we carried our tests with a 5400-rpm hard disk and measured the vibration profile along the diameter of the disk. A typical vibration profile of any mechanical system comprises of fundamental rotational frequency with additional harmonics. As expected, the frequency detected were 90Hz,180 Hz and 270Hz. (Fig. 10). The peak to peak wobble increases 0.28μm/mm linearly along the diameter from the centre to the periphery. On loosening the mounting screws of the hard-disk, the offset wobble increases as well as the slope i.e. wobble along the diameter increases to 0.5μm/mm.(Fig.11)

iv) Measurement with targets of varied roughness & curved surface

Metallic target objects with different surface roughness were used for vibration. Vibration of plain surfaces with roughness varying from 0.025 μm Ra to 0.2 μm and also with parallel and criss-cross finish was monitored. The target surfaces were placed at a standoff distance of 15 mm. The outputs of the measurements remained fairly consistent with applied
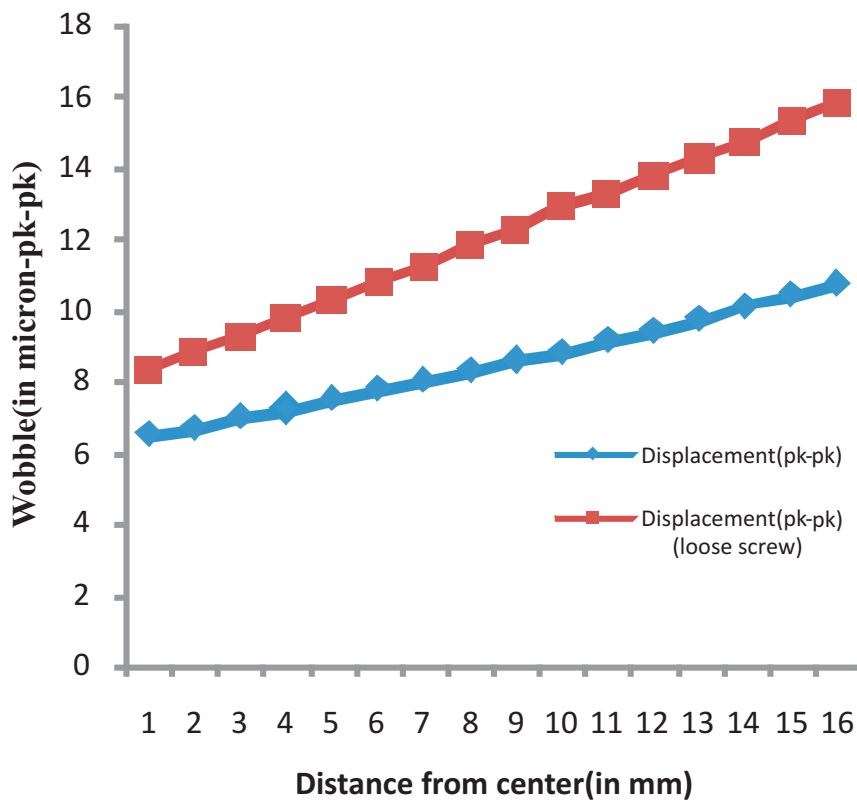
Fig.11. Wobble vs. Distance along Diameter

excitation. Similarly, for a curved surface with a radius of 22 mm, roughness of Ra 0.025 µm, CLA :1µin, and Classe N1, single tone piezo excitation was applied. The frequency of excitation was 20Hz. The probe was placed at a standoff distance of approximately 10 mm. As observed, the measured displacement was 5.418µm(pk-pk) at 20 Hz. Additionally, a 40 Hz component in the spectrum was found as a harmonic of the vibrating frequency owing to the mechanical mounting of the structure.

Discussion

Preliminary experiments were conducted to measure misalignment of shafts and targets with different roughness. Thus, the sensor can be used for alignment monitoring applications. The sensor can used for reflective targets with varying roughness and is suitable for non-contact probe based measurements with a standoff distance ranging from 5 mm to 5 cm. Laboratory demonstration of detection of multi frequency dynamic displacements and wobble measurements indicate the usefulness of the sensors in vibration monitoring applications where misalignments/loosening generate harmonics of fundamental rotational frequencies[13].

The performance metrics obtained were validated against the piezo stack datasheets. Piezo stacks typically offer picometer range of accuracy. The sensor was tested without any temperature or pressure compensation. Further improvements to the sensor involve calibration, compensation and control of temperature and other ambient fluctuations which shall improve the accuracy of the sensor.

Conclusion

A low-cost fiber-based sensor based on FPI for vibration sensing applications has been developed. The sensor was tested to measure displacements in the range of 200 nm to 15 µm pk-pk. The sensor showed a standard deviation of 2%, a resolution of 12 nm and a precision of 1.4 nm when tested with a piezo actuator of stroke length of 9 µm. The sensor can also measure derived parameters like velocity and acceleration. Use of fiber optic probes makes it suitable for measurement of vibration or dynamic displacements in EMI/EMC environment and radiation areas. Fiber optic cables at 1550 nm offer very low attenuation, are available commercially and thus can be used for remote sensing. The sensor was demonstrated to measure wobble and multi frequency displacements with spectrum analysis features, hence suitable for online vibration monitoring applications.

*Corresponding author

Shri Nitin Kawade

References

1. IRD811D O&M manual , IRD Mechanalysis Limited, Available: https://www.irdmech.com/User%20Manuals/IRD811D%20User%20Manual%20v2.3Sept15.pdf, accessed on :21 July, 2020.

2. Vibration Monitoring Solutions(Application note), Wilcoxon Sensing Technologies available: https://wilcoxon.com/wp-content/uploads/2019/01/Application-solution_Nuclear-Power-Plant.pdf accessed on :21 July,2020.

3. Blevins, R. D. , 1979a, "Flow-Induced Vibration in Nuclear Reactors: A Review," Prog. Nucl. Energy 0149-1970, 4(1), pp. 25–49. Available: https://doi.org/10.1016/0149-1970(79)90008-8.

4. Hashemian, H. M. (1994) "Fiber optic sensors for nuclear power plants." United States: N. p., Available:https://www.osti.gov/biblio/54585-fiber-optic-sensors-nuclear-power-plants.

5. Shrikant Maske; A. D. Shaligram; P. B. Buchade.(2018), "A novel fiber bundle configuration for concurrent improvement of displacement range and sensitivity of self-referenced fiber optic displacement sensor",Optics & Laser Technol.,98,339-343. Available : http://doi.org/10.1016/j.optlastec.2017.08.006.

6. J. Binghui and Z. Junhua, 2018,"Design on a Common-path Precision Fiber Optic Displacement Sensor," 2018 15th International Conference on Ubiquitous Robots (UR), Honolulu, HI, pp. 863-866, Available : https://doi.org/10.1109/URAI.2018.8441873.

7. A. Rathod, S. Mishra, S. Ghindiyal, S. K. Bahuguna, S. Dhage, S. Mukhopadhyay, [2013] "Development of DSP based signal acquisition and processing system for EFPI fiber optic sensors", BARC Newsletter, Issue no. 330.

8. Chen, W.; Feng, F.; Chen, D.; Lin, W.; Chen, S.-C. 2019, "Precision non-contact displacement sensor based on the near-field characteristics of fiber specklegrams." Sens. Actuator A 296, 1–6. Available: https://doi.org/10.1016/j.sna.2019.06.010.

9. Klaus Thurner, Francesca Paola Quacquarelli, Pierre-François Braun, Claudio Dal Savio, and Khaled Karrai. (2015),"Fiber-based distance sensing interferometry," Appl. Opt. 54, 3051-3063. Available: http://doi.org/10.1364/AO.54.003051.

10. Acharya, Anisha & Kawade, Nitin. (2020). "A Fabry-Perot Interferometer based Fiber Optic Dynamic Displacement Sensor with an Analog In-phase/Quadrature Generator." IEEE Sensors Journal. PP. 1-1. Available : https://doi.org/10.1109/JSEN.2020.3009587.

11. J. L. Santos, A. P. Leite, and D. A. Jackson.(1992),"Optical fiber sensing with a low-finesse Fabry–Perot cavity," Appl. Opt. 31, 7361-7366 Available: http://doi.org/10.1364/AO.31.007361.

12. A. Dandridge, A.B. Tveten, T.G. Giallorenzi. (1982), "Homodyne demodulation scheme for fiber optic sensors using phase generated carrier",IEEE Trans. Microw. Theory Tech., 30, pp. 1635-1641. Available: http://doi.org/10.1109/TMTT.1982.1131302.

13. P. E. S. Goldman, "Vibration spectrum analysis: A practical approach", New York: Industrial Press,1999, pp. 83-90.

ANUSim - The Nuclear Chemical Processes and Equipment Simulator

Mayur Darekar, Sourav Sarkar, K.K. Singh*, S. Mukhopadhyay, K.T. Shenoy
Chemical Engineering Division
Venkata P.P.K.
Computer Division
Sadhana Mohan
Chemical Engineering Group

Abstract

This work reports initiation of development of a software named ANUSim which will serve as a simulator for chemical processes used in the nuclear fuel cycle and the equipment used in these processes. ANUSim will have a modular structure with different modules catering to different chemical processes or equipment. The first module that has been developed is the Liquid-Liquid eXtraction Cascade Simulator (LLXCSim). This module can be used to simulate multistage counter-current cascades for extraction, scrubbing and stripping operations. It can be used to either calculate the number of stages in a cascade required to achieve desired exit concentrations or exit concentrations for a given number of stages. At present, mass transfer of up to two components having constant or variable distribution coefficient can be simulated. Aqueous and organic phases are considered immiscible. The module has been validated with reported literature data.

Keywords: ANUSim, Liquid-Liquid eXtraction Cascade Simulator (LLXCSim), Simulator, Simulations, Codes, Multistage liquid-liquid extraction cascades, Chemical engineering, Isotope separation, Nuclear desalination.

Introduction

Chemical engineering plays an important role in the entire nuclear fuel cycle, right from mining of uranium ore to production of nuclear grade uranium, processing of spent nuclear fuel and waste management. This cradle-to-grave journey of nuclear fuel involves many specialized processes and equipment which need to be designed optimally. Chemical engineering is important in many other processes directly or indirectly related to the nuclear fuel cycle such as separation/ purification of nuclear materials, isotope separation, hydrogen production, solvent synthesis, nuclear desalination, etc. The overwhelming use of chemical engineering in nuclear industry calls for codes and simulators that can be used to simulate different

processes and optimally design the equipment used therein. Though there are several commercial simulators, they are mainly focused on processes and equipment used in chemical process industry and petrochemical industry. For example, commercial simulators have better capabilities to simulate distillation than liquid-liquid extraction as distillation is more common in chemical process industry and oil and gas industry. Whereas, liquid-liquid extraction is the most commonly used separation process in nuclear fuel cycle (Eccles et al., 2000, Jassim et al 1984, Mathur et al., 2001, Singh and Gupta 2000). Also, several processes for producing materials required in nuclear industry such as heavy water are very specific and cannot be simulated using commercial simulators. In general, commercially

available simulators are oriented to cater to the requirement of non-nuclear chemical process industry and oil and gas industry. To meet the requirement of simulating chemical processes and equipment relevant to nuclear industry, it is proposed to develop a simulator named as ANUSim. ANUSim will provide a platform for integration of codes written by different researchers under one umbrella with proper packaging which will include an attractive user-friendly Graphical User Interface (GUI) and detailed documentation. ANUSim will aim to ensure that the codes developed by different researcher are permanently archived in useable form and perpetually available. The ANUSim will have a modular structure. Each module will cater to a specific process or process
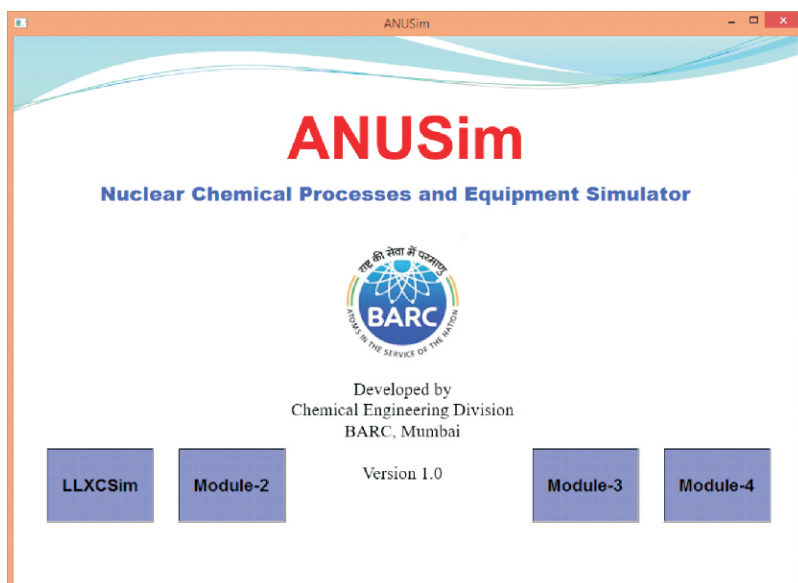
Fig.1: Welcome screen of ANUSim

Fig.2: The four options in LLXCSim module
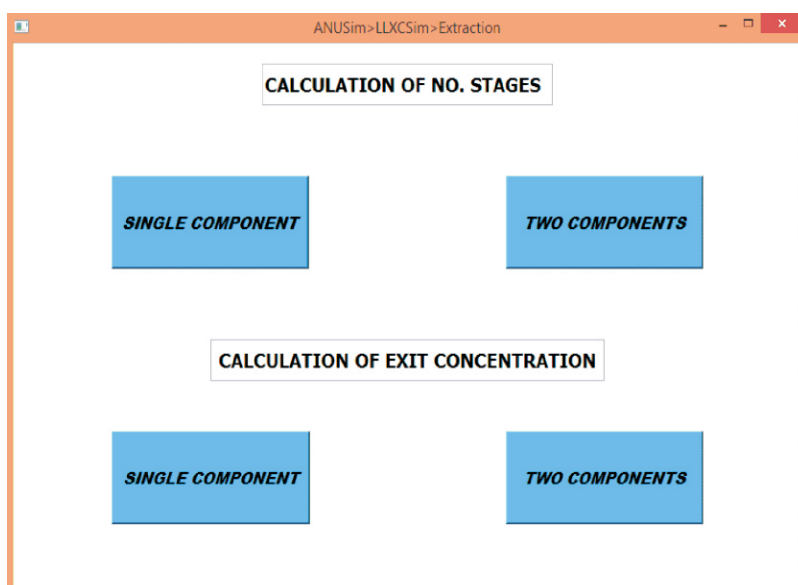
Fig.3: Snapshot of the GUI of extraction module under LLXCSIM

equipment. The snapshot of the first screen of ANUSim is shown in Fig. 1. Liquid-Liquid eXtraction Cascade Simulator (LLXCSim) is the first module of ANUSim. Other modules are under development.

Overview of LLXCSim

Liquid-liquid extraction is extensively used in both the front-end and the back-end of nuclear fuel cycle. Multistage liquid-liquid extraction cascades using stage-wise contactors such as mixer-settlers, slurry extractors and centrifugal extractor are common in nuclear industry. A typical solvent extraction process involves extraction, scrubbing and stripping operation. To achieve required percentage extraction of the desired component(s) for a given processing rate, the number of stages needs to be calculated. In some plant retrofitting cases, number of stages is known and exit concentration(s) need to be calculated. Also, each stage might have a finite efficiency depending on the design and operating conditions. All these factors are taken into the consideration in LLXCSim. On clicking LLXCSim tab in the welcome screen of ANUSim, the user is taken to the next page which offers 4 different options i.e. simulation of only extraction cascade, only stripping cascade, extraction-stripping cascades and extraction-scrubbing-stripping cascades as shown in the snapshot given as Fig. 2.

On choosing "EXTRACTION" or "STRIPPING" options shown in Fig. 2, the user reaches the next page snapshot of which is shown in Fig. 3. The user can now opt for either calculation of number of stages if exit concentration is provided or opt for

Table 1: Different types of cascade simulations possible with LLXCSim

Extraction	Number of stage calculation	Single component
		Two components
	Exit concentration calculation	Single component
		Two components
Stripping	Number of stage calculation	Single component
		Two components
	Exit concentration calculation	Single component
		Two components
Extraction-Stripping	Exit concentration calculation	Single component
		Two components
Extraction-Scrubbing-Stripping	Exit concentration calculation	Single component
		Two components

Fig.4:Snapshot of the GUI of LLXCSim for estimating number of stages for extraction of a single component

calculation of exit concentration if number of stages is provided. For either case, user can opt for single component or two components. "EXTRACTION STRIPPING" and "EXTRACTION SCRUBBING STRIPPING", shown in Fig. 2, work with predefined cascades in which user fixes the number of stages in the different cascades and concentrations in the exit streams are calculated. Different types of simulations possible with LLXCSim are listed in Table 1. In all cases constant or variable distribution coefficient can be used.

Simulation of Extraction Cascade

Simulation of extraction cascade is described in this section to showcase the typical features of LLXCSim. The snapshot of the GUI used for calculation of number of equilibrium stages for single component extraction is shown in Fig. 4. Flow rates of the aqueous and the organic phase, the inlet concentrations of the component in the aqueous phase and organic phase and the desired concentration in raffinate need to be specified by the user. The software calculates number of stages (N_a). The equilibrium relation (distribution coefficient) in the form of a polynomial relating the concentration of the component in the aqueous phase in equilibrium with concentration of the component in organic phase is to be provided by the user. Constant distribution coefficient can be used by putting the coefficient of $(Ca)^1$ equal to the distribution coefficient value and other coefficients as zero in the polynomial equation.

The stage efficiency (E_m) is also specified by the user. On clicking compute button, number of stages and concentration of the component in the loaded organic stream are calculated and filled in the respective blank fields in the GUI. At the end of the calculation, overall material balance of the component is checked and displayed. After calculation of number of stages, plot of equilibrium line, operating line and stages can be seen by clicking "Graph" button of the GUI shown in Fig. 4. The typical plot is
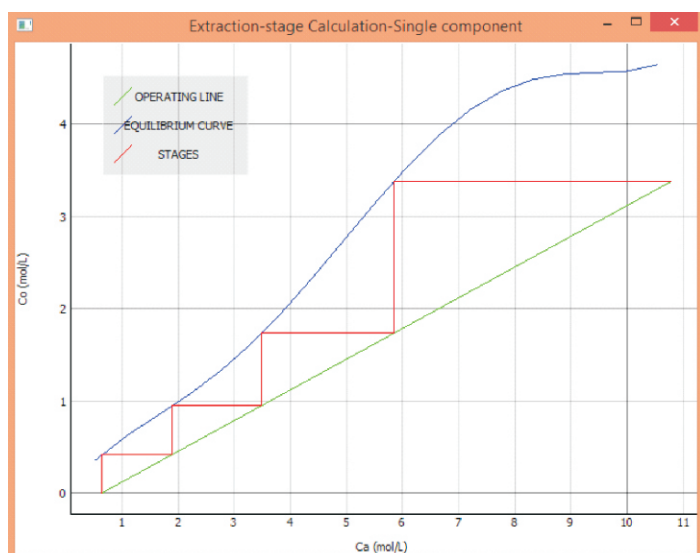
Fig.5: Graphical representation of the number of stages, operating line and equilibrium curve
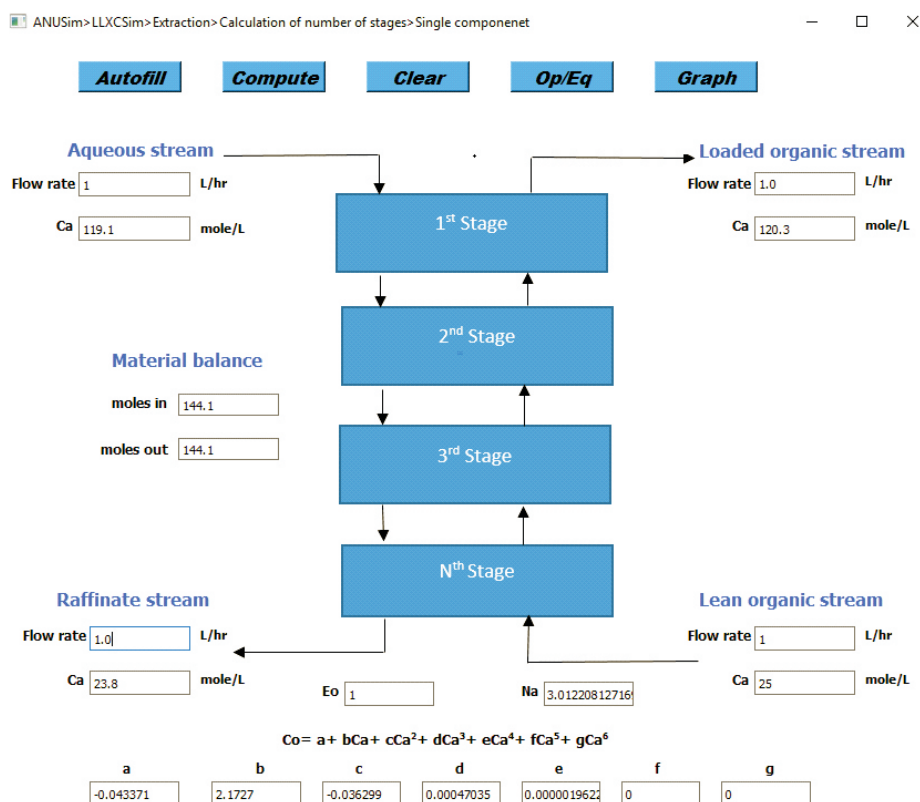
Fig.6: Snapshot of LLXSim used to simulate the data of Banda et al., 2012

shown in Fig. 5. The "Autofill" button is provided in the GUI. When the user clicks this button, the inputs fields are filled by some preset values. If required, these preset values can be modified by the user. This feature helps the user save the time required to manually fill each and every input field when the user is a beginner and

just getting familiar with the GUI. By clicking "op/equ" user can also check the operating line and equilibrium curve before calculating number of stages. This helps the user to know whether for the specified input data, the operating line and equilibrium curve intersect or not. The two phases are assumed to have negligible mutual

solubility. Due to this the flow rates of the aqueous and organic streams remain constant. The software can be modified if other functional forms of equilibrium relation or mutual solubility of aqueous and organic phases need to be considered by a user. As of now the LLXCSim needs thermodynamic data as user input. Work is in progress for developing sub-modules of LLXCSim for specific processes of nuclear fuel cycle. Such process specific sub-modules will embed all relevant thermodynamic data with only flow rates and feed compositions left as the user inputs.

Validation

LLXCSim has been tested by comparing its predictions with the results of manual calculations. Additionally, validation of LLXCSim has been done using the reported experimental data. Banda et al., 2012 have reported graphical stage calculation for extraction of Praseodymium (Pr) using organic phase consisting of 1M saponified Cyanex 272 and 0.5% TBP. The operating line in the graphical calculation of Banda et al. shows that Pr concentration can be brought down from 119.1 unit to 23.8 unit in a counter-current cascade consisting of 3 stages. The concentration of Pr in the organic phase at the feed-end and raffinate-end are 120.3 unit and 25 unit, respectively. Ratio of organic phase flow rate to aqueous phase flow rate is 1/1. LLXCSim module of ANUSim was used to simulate counter-current cascade for extraction of Pr. Discrete equilibrium data points provided by Banda et al. were used to fit a polynomial relating Pr equilibrium concentration in the organic phase and the aqueous phase.

This polynomial equation was used in LLXCSim.

The aqueous phase and organic phase flow rates, Pr concentration in the incoming aqueous and organic phase were keyed in and the number of stages required to bring down Pr concentration from 120.3 unit to 25 unit was calculated. As shown in Fig. 6, the number of stages calculated by LLXSim is 3.01 which compare very well with the number of stage obtained graphically by Banda et al. Concentration of Pr in the extract as obtained from LLXCSim is 120.3 unit which also matches perfectly with the extract concentration estimated graphically by Banda et al.

Conclusion

A software named as ANUSim is proposed as a simulator for nuclear chemical processes and equipment used in them. The software will have a modular structure to cater to different chemical processes and equipment. It will have a user-friendly graphical user interface (GUI). This study reports the development of the first module of ANUSim for simulation of counter-current liquid-liquid extraction cascades. This module has been named as LLXCSim. The capabilities and features of LLXSim are discussed and validation with reported literature data is presented.

The work is underway to develop other modules such as module for fluidized bed thermal denitration of ammonium nitrate, module for population balance modeling of liquid-liquid stirred dispersions and modules for air pulsed columns. A process simulator like ANUSim will be very useful for the designers and practicing chemical engineers in nuclear industry. ANUSim will also provide a platform to integrate the computer codes developed by individual researchers under one umbrella. This will help in archiving the knowledge generated by individual researchers properly and making it perpetually available to nuclear chemical engineer fraternity.

*Corresponding author

Dr. K.K. Singh

References

1. Banda R., Jeon H., Lee M. "Solvent extraction separation of Pr and Nd from chloride solution containing La using Cyanex 272 and its mixture with other extractants". Separation and Purification Technology, 98 (2012) 481-487.

2. Jassim T. M., Liljenzin J. O., Lundqvist R., Person G. "Co extraction of uranium and technetium in TBP-systems". Solvent Extraction and Ion Exchange, 2(3) (1984) 405–419.

3. Eccles H. "Nuclear fuel cycle technologies: Sustainable in the twenty-first centuryfi". Solvent Extraction Ion Exchange, 18(4) (2000) 633–654.

4. Mathur J. N., Murali M. S., Nash K. L. "Actinide partitioning: A review". Solvent Extraction and Ion Exchange, 19(3) (2001) 357–390.

5. Singh H. and Gupta C. K. "Solvent extraction in production and processing of uranium and thorium". Mineral Processing and Extractive Metullargy, 21(1-5) (2000) 307-349.